LA-UR-17-25600
Approved for public release; distribution is unlimited.

Title: Soft X-ray spectrometer design for warm dense plasma measurements on DARHT Axis-I

Author(s): Ramey, Nicholas Bryan
Perry, John Oliver
Coleman, Joshua Eugene

Intended for: CWRU Senior Thesis

Issued: 2017-07-11

Soft X-ray spectrometer design for warm dense plasma measurements on DARHT Axis-I

N.B. Ramey[1,2], J.O. Perry[1] & J.E. Coleman[1]

[1]*Los Alamos National Laboratory, Los Alamos, NM, USA*
[2]*Department of Physics, Case Western Reserve University, Cleveland, OH, USA*

05 May 2017

Abstract

A preliminary design study is being performed on a soft X-ray spectrometer to measure K-shell spectra emitted by a warm dense plasma generated on Axis-I of the Dual-Axis Radiographic Hydrodynamic Testing (DARHT) facility at Los Alamos National Laboratory. The 100-ns-long intense, relativistic electron pulse with a beam current of 1.7 kA and energy of 19.8 MeV deposits energy into a thin metal foil heating it to a warm dense plasma. The collisional ionization of the target by the electron beam produces an anisotropic angular distribution of K-shell radiation and a continuum of both scattered electrons and Bremsstrahlung up to the beam energy of 19.8 MeV. The principal goal of this project is to characterize these angular distributions to determine the optimal location to deploy the soft X-ray spectrometer. In addition, a proof-of-principle design will be presented. The ultimate goal of the spectrometer is to obtain measurements of the plasma temperature and density to benchmark equation-of-state models of the warm dense matter regime.

Contents

Chapter 1

Introduction

Figure 1.1: The DARHT facility at Los Alamos National Laboratory [1].

Figure 1.2: The DARHT Axis-I single pulse electron linear induction accelerator and pulsed power hall [2].

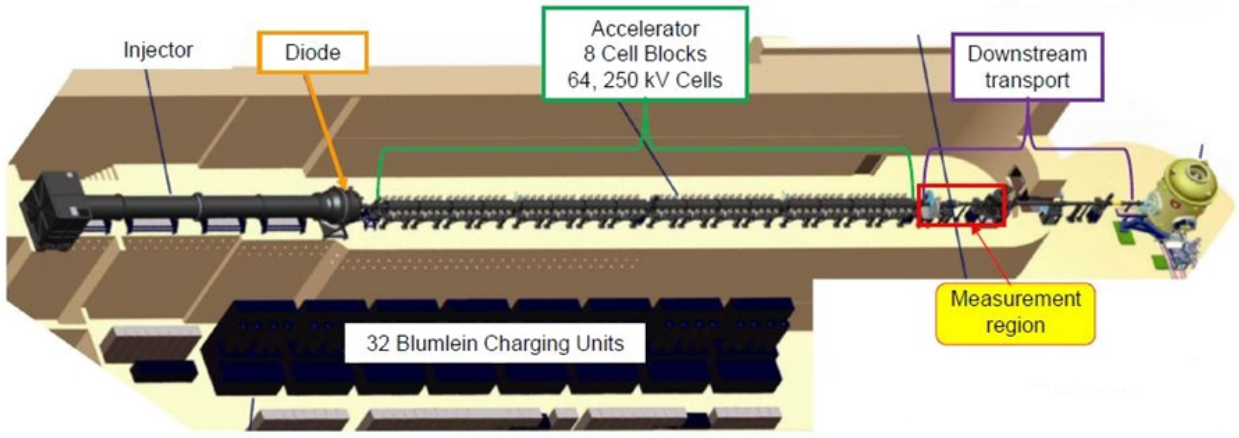

1.1 The Dual Axis Radiographic Hydrodynamic Testing Facility

The Dual Axis Radiographic Hydrodynamic Testing (DARHT) facility (Figure 1.1) at Los Alamos National Laboratory (LANL) is a dual-axis electron accelerator that serves the Department of Energy's Stockpile Stewardship Program. Each electron beam is focused onto a high-Z target that converts the particle beam energy into X-rays. DARHT's two orthogonal accelerators deliver multiple X-ray pulses (1 from Axis-I and 4 from Axis-II) to obtain high-speed radiographs of materials moving $\sim$1 km/s.

DARHT Axis-I produces a single 80 ns FWHM, intense relativistic electron bunch with an energy of 19.8 MeV and a nominal current of 1.7 kA. A 4 MeV injector extracts electrons from a velvet cathode and 64 accelerator cells add kinetic energy to the beam through the length of the accelerator to reach an energy of 19.8 MeV (Figure 1.2). Axis-I has a flexible range of fluence by adjusting the number of accelerator cells used or cathode size. We are currently operating with a 50-mm-diameter cathode to produce a 1.7 kA beam for the beam-target interaction studies and WDM experiments.

WDM studies are currently underway on Axis-I to study and characterize the expanding

Figure 1.3: The measurement region (from Figure 1.2) of the Axis-I downstream transport, including the DT1 focusing solenoid and diagnostic chamber with viewports that houses the WDM experiments [2].

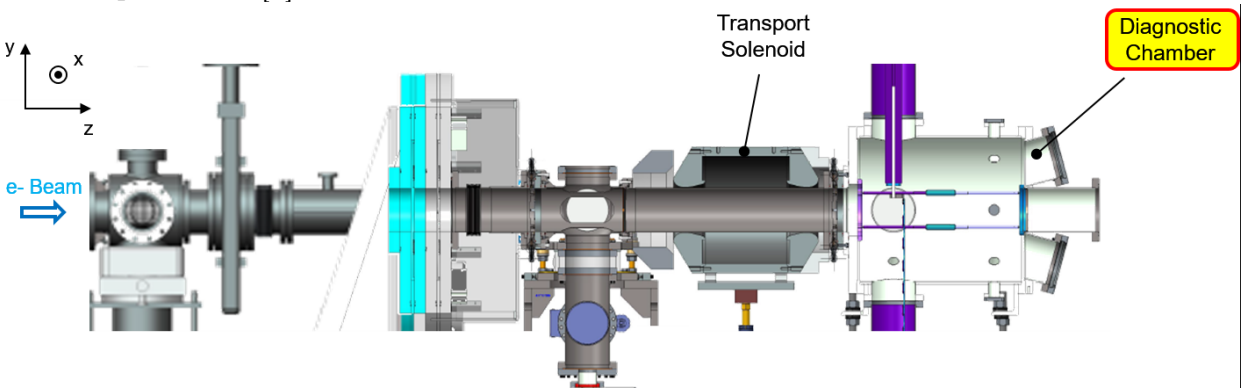

plasma. Figure 1.3 shows the downstream section of Axis-I where the studies are taking place. The goal of these studies is to provide a temporal and spatial measurement of the plasma plume expansion and the beam spot. The targets are 100-μm-thick foils with materials ranging from C to Au, although we are primarily focusing on $Z < 29$. At present, we are only testing low-Z materials (Al, Ti, Fe, Ni, and Cu) to minimize Bremsstrahlung production at the target and to better understand the physics of the interactions at hand. Our generation of warm dense plasma using relativistic electrons as a collisional heating mechanism is the first of its kind and provides a controlled environment from which to study WDM. We are currently only depositing <1% (∼10 J in a Ti foil) of available beam energy into the target, which affords flexibility for future studies that involve generating and characterizing various phases of plasma [2].

1.2 WDM Regime EOS

WDM is the region in temperature (T) – density (ρ) space where 0.1 eV $< T <$ 10 eV and $0.1 < \rho/\rho_0 < 10$ with ρ_0 the solid density of the material. Shown in Figure 1.4 is a phase diagram of a plasma generated from aluminum and a plot illustrating the time evolution in phase space of our plasma on Axis-I. The state of WDM is not described well by normal

Figure 1.4: a Temperature-density plot of an aluminum plasma indicating the location of the WDM regime [2]; b) WDM Temperature-density plot detailing the time evolution of an Al plasma generated on Axis-I. The near-solid density and resulting opacity of the WDM requires using the emitted soft X-rays to determine T_e and n_e [4, 5].

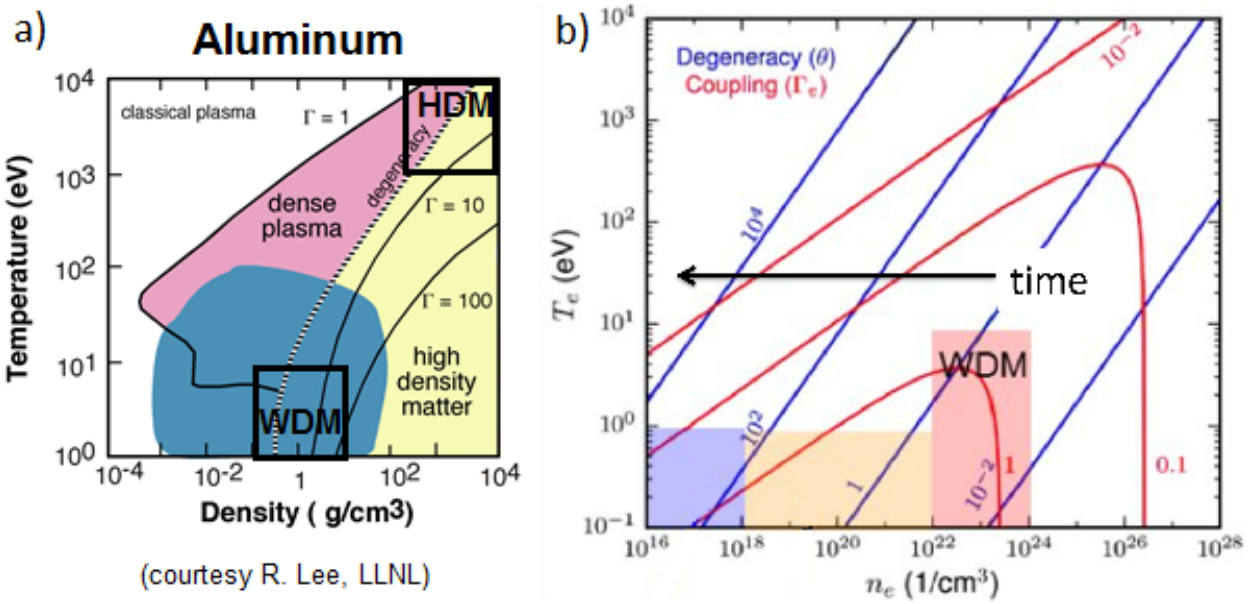

condensed matter theory or by weakly-coupled plasma theory. To accurately characterize this state, all classical and quantum effects must be taken into consideration [3]. The goal of the WDM experiments is to benchmark existing EOS models of the warm dense plasma generated at the target during the beam pulse.

In order to develop a model of the WDM regime EOS, the following plasma properties must be measured: electron temperature (T_e), electron density (n_e), and pressure (P). The diagnostic suite on DARHT Axis-I includes the following: visible spectroscopy (Doppler broadening, ionization states, Stark broadening), plasma plume imaging, interferometry (Moiré diffractive imaging, Talbot-Lau, Mach-Zehnder, Nomarski), and Photon Doppler Velocimetry (PDV).

Visible spectroscopy and Thomson scattering can provide spatially-resolved measurements of n_e and T_e in a lower-density plasma given a proper optics setup. X-ray spectroscopy and Thomson scattering are more likely to provide measurements of the warm dense plasma

and can be spatially resolved if paired with collimators and the right detectors. We can achieve more precise spatial measurements of n_e using the aforementioned interferometry techniques. PDV will provide the most reliable and absolute measurement of the hydrodynamic disassembly time for the expansion of the target plasma. Measurements of the expansion velocity of the plasma plume will allow for the plasma pressure to be determined [6].

Design of an X-ray spectrometer affords the possibility of measuring both n_e and T_e of the warm dense plasma, but the effectiveness of this diagnostic depends on the spatial distribution of both the emitted X-rays by the plasma and the Bremsstrahlung radiation generated in the target region [7]. Fielding a soft X-ray diagnostic on a Bremsstrahlung machine the category of DARHT has never been done before and will be difficult. Specifically, the X-ray spectrometer will be measuring the K-shell lines emitted by the plasma during the WDM phase early in time; this will consist of the K-α and K-β lines. Intensity and width measurements of these lines (with proper calibration) and their ratios to one another with numerical models will allow us to directly determine the electron density and temperature of our warm dense plasma. However, the energy range we intend to measure ($<$10 keV for $Z < 29$) is orders of magnitude smaller than the Bremsstrahlung continuum, which can have energies up to the beam energy of 19.8 MeV.

Chapter 2

Objectives

To design an X-ray spectrometer that will function efficiently in a high-energy Bremsstrahlung environment presents significant challenges. A review was performed of various spectrometer geometries and environments in which they are deployed to help successfully accomplish this goal. The scope of this project will consist of:

1. Evaluate the X-ray energy range of interest based on target materials.
2. Characterize the polar distributions of K-line spectra, Bremsstrahlung, and scattered electrons.
3. Layout spectrometer and detection techniques under consideration.
4. Perform a preliminary design of the most practical case and layout plans for a proof-of-principle measurement.

This research will be ongoing into Summer 2017 when I return to LANL to continue my work. The plans for the proof-of-principle measurement should be realized at that time. Consequently, the primary goal of this project while I am still at CWRU is to thoroughly characterize the scattered X-rays and electrons using the results of Monte Carlo simulations to better inform us of the design space associated with each material tested. The ultimate goal of this spectrometer is to measure emitted K-shell spectra of various low-Z materials. The information gained from these measurements will provide a measurement of the temperature and density of the warm dense plasma. This data, combined with the current

diagnostic suite on Axis-I, will provide a detailed understanding of the time evolution of WDM and possibly improve radiographic quality at DARHT.

Chapter 3

Spectrometers and Detectors

There exist a wide variety of X-ray spectrometers that can measure across a breadth of energies. In addition, the type of detector used can determine the kind of measurement obtained, namely time resolution or spatial resolution of the X-ray energies. Certain techniques work better in a certain energy range, as will be shown below. I will divide the types of spectrometers in the following way: K-edge and Ross Filtering, Transmission Geometries, and Reflection Geometries. A brief summary of each spectrometer technique will be included along with preliminary comments to illustrate the possible advantages and disadvantages of deploying each on DARHT Axis-I.

3.1 K-edge and Ross Filtering

K-edge filtering is a simple technique used to measure X-rays in a known energy range without the presence of a high-energy background. It consists of a thin foil of a metal or other compound with a known thickness. A K-edge filter either (a) passes X-ray energies at or slightly below the characteristic K-β or (b) filters out energies greater than the characteristic binding energy of the atoms (Figure 3.1a). This attenuation of photons with energies above the K-edge is due to the photoelectric absorption of the incident photons. A Ross filter, also known as a Ross pair, is a band-pass filter formed by a pair of K-edge filters of different

Figure 3.1: a) Transmission curve of a 10-μm-thick Fe K-edge filter as a function of incident X-ray energy. It is observed that as the energy of the X-ray increases to much larger than the K-edge, the transmission approaches unity [9]; b) A Ross pair created by matching the leading and trailing K-edge curves of two relatively adjacent metals on the periodic table [10]. For large incident X-ray energies, the transmission goes to unity.

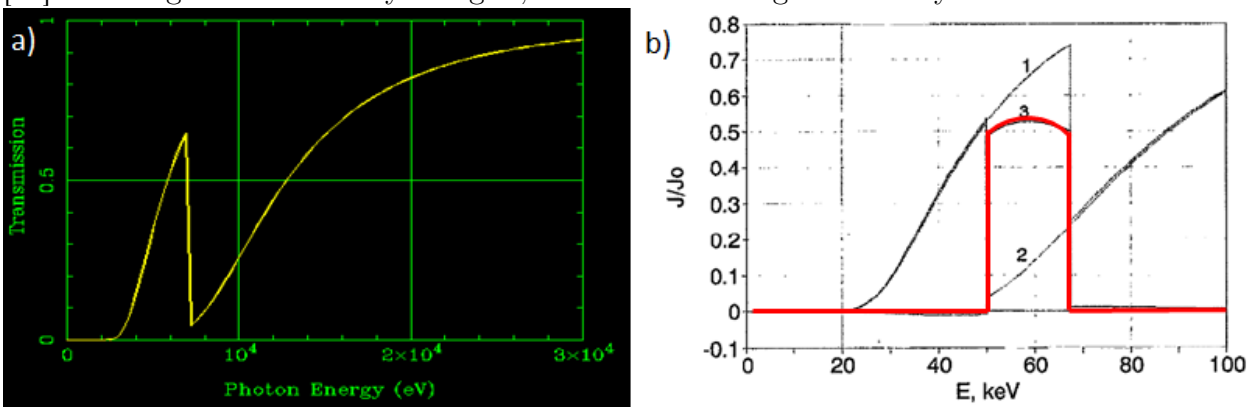

materials. The required condition of a Ross filter is the matching of the leading and trailing slopes of the constituent K-edge filters, which results in a band-pass filter operating in the energy range spanned by the filters' respective K-edges (Figure 3.1b) [8].

The advantage of K-edge filters and Ross pairs is the ease of fabrication and implementation as they can be easily located and used in conjunction with a detector of choice. However, as the energy of incident X-rays increases to much larger than the K-edge value, the transmission approaches 100%. This proves problematic for our situation as we want to measure energies $<$10 keV but the Bremsstrahlung background can reach up to 20 MeV. However, they could be useful in conjunction with other types of spectrometer techniques to further restrict the energy range of interest. A possible use that is beyond the scope of this project but would provide valuable information to future diagnostic design on DARHT Axis-I is to use an array of K-edge filters with diamond radiation detectors to map out the spatial and energy distribution of the scattered Bremsstrahlung radiation.

Figure 3.2: A diagram of a typical transmission grating spectrometer. The Be K-edge filter it used to remove low energy X-rays and visible light. If the grating were replaced by a transmission crystal, this would represent a Laue geometry.

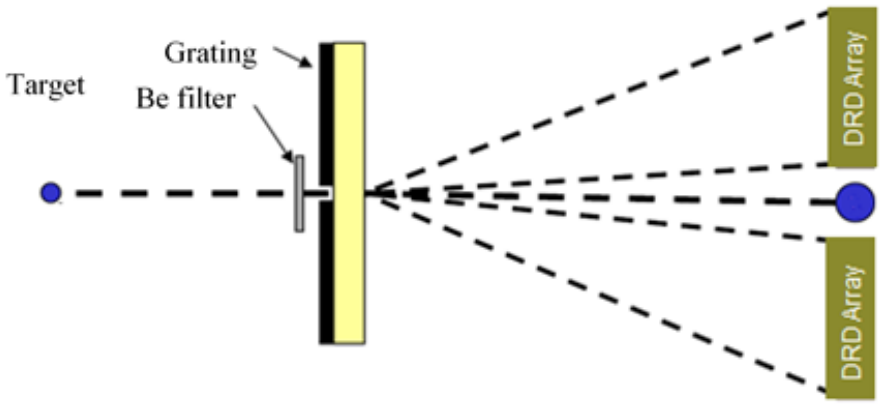

3.2 Transmission Geometries

A Transmission Grating Spectrometer (TGS) operates by using a diffraction grating to separate out X-rays by their energies (Figure 3.2). It uses a pinhole to focus the X-rays before passing through the grating. The location of the various energies on the detection plane can be easily calculated from the equation for constructive interference once fixing the following parameters: grating period, grating-detection plane distance, and X-ray energy. The biggest limitation in our design requirements with using a TGS is the range of energies of interest paired with the grating period required to resolve the energies. This was discovered through a feasibility study for a soft X-ray TGS. Because of our wavelengths of interest for low-Z ($\sim$1–10 Å), a commercially available transmission grating will have difficulty discriminating between the soft X-rays we wish to measure. For example, the distance between first maxima of Cu K-α_1 and K-β_1 lines (8047 and 8905 eV, respectively [11]) on the detection plane for a TGS with grating period of 50 nm and grating-detection plane distance of 1 m is only 300 μm. This is obtained by using the equation $m\lambda = d\sin\theta$ where $\lambda = hc/E$, d is the grating spacing, and θ is the angle with respect to the normal of the diffracted X-ray. As a result, an effective TGS would need to be paired with a detector capable of resolving peaks at this scale (one candidate might be a Gated X-ray Imager).

Figure 3.3: A bent crystal (Cauchois) geometry [12]. Note the location of the detector with respect to the undiffracted X-ray paths.

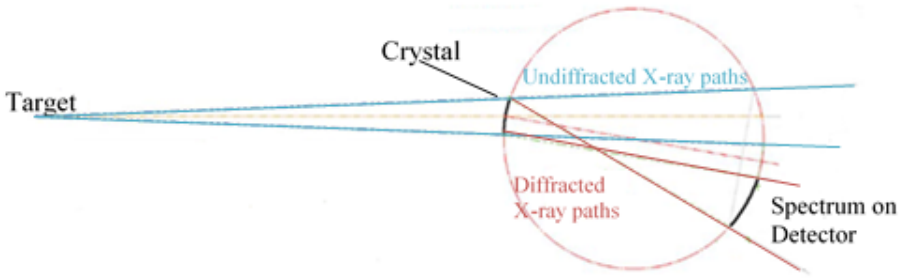

There exist two common transmission crystal geometries. A Laue geometry uses a planar crystal with the plane of diffraction oriented normal to the incident X-ray direction of propagation to diffract X-rays similar to a TGS (refer to Fig. 3.2). A Cauchois geometry uses a cylindrically bent crystal and correspondingly curved diffraction plane to diffract incident X-rays (Figure 3.3). The crystal and detection plane lay on the perimeter of what is known as a Rowland Circle (RC), where the radius is identical to the radius of curvature of the crystal. The spatial resolution of a Cauchois geometry can be enhanced to an extent by moving the detection plane radially outward (the curved detection plane lies outside of the RC) [13, 14].

The greatest advantage a transmission crystal geometry offers is the much finer grating (atomic lattice) that can more efficiently diffract soft X-rays. Furthermore, a Cauchois geometry allows for the detector to be placed out of the line of sight of the target, which can help diminish background Bremsstrahlung reaching the detector. The primary disadvantage of transmission crystal geometries is the absorption of the crystal, which is significant around or below 7 keV. The exact coefficients of transmission of various crystals can be calculated using the Henke tables from the Center for X-ray Optics in Lawrence Berkeley National Laboratory's Materials Science Division.

3.3 Reflection Geometries

A Bragg spectrometer uses a Bragg crystal to diffract the incident X-rays according to Bragg's law. This geometry typically then results in a detection plane that is not oriented orthogonally with respect to the X-rays incident on the crystal. In our case, this is beneficial as it allows the detectors to be out of the line of sight of the source, thus cutting down on the potential Bremsstrahlung background present at the detection plane. A reflection-type geometry becomes inefficient with an increase in photon energies. This is due to the following: the integrated reflectivity of the crystal generally decreases with decreasing Bragg angle, decreasing lattice spacing (dependent on the type of crystal), and increasing diffraction order number [8]. However we are considering a low enough energy range as well as keeping a larger Bragg angle so this will not be an issue.

Bragg angles approaching the maximum of $\Theta_B = 45°$ would be ideal for deployment on DARHT Axis-I as it would allow us to locate the detector in the region of minimum Bremsstrahlung background intensity [7]. We can stay close to this angle by using multiple crystals. The difficulty in using a Bragg geometry is the limitation on the number of viewports present in the vacuum diagnostic region. A proof-of-principle design of a Bragg spectrometer will be presented in Chapter 5, where the placement of the crystal will be guided by the results of the Monte Carlo simulations which determine the spatial distribution of emitted soft X-rays by the target.

3.4 Detection Techniques

Detector type and size will directly determine the measurement obtained by the spectrometer chosen. Optical measurements and energy deposition profiles indicate the 100-μm-thick foils are in the warm dense phase at t>50ns up to 100ns so we need to choose a detector with a quick response time in order to capture the emitted soft X-rays [15]. There are three possible candidates: diamond radiation detectors (DRDs), PIN diodes, and a Gated X-ray Imager

(GXI) [16].

Figure 3.4: a) SMA casing that houses a single DRD. The DRD can be paired with shielding as required (ex.: graphite, Al, W). b) The Tektronix bias tee with a fast response time coupled with the DRD to hold charge [21].

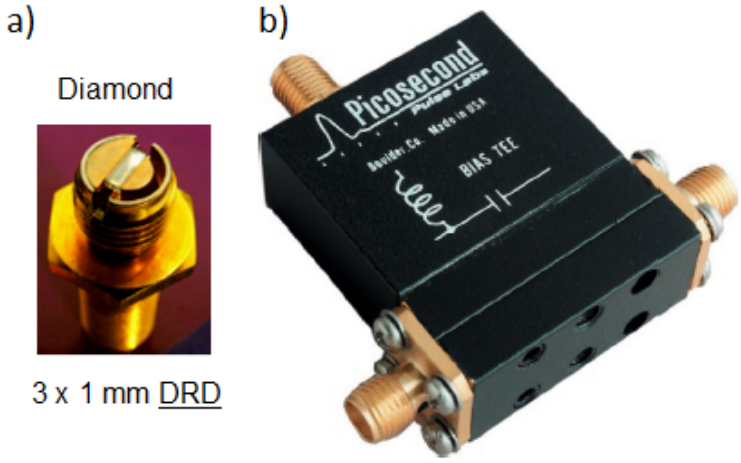

3.4.1 Diamond Radiation Detectors

DRDs, also known as photo-conductive detectors (PCDs), are radiation hardened detectors with a spectrally flat response (Figure 3.4a) [17]. They have extremely quick rise and fall times (∼200 ps) which makes them excellent for obtaining time-resolved spectra [18]. Diamond possesses a band gap of 5.5 eV and has a very small absorption coefficient for incident photons below this energy [19]. DRDs are capable of measuring any type of radiation that can generate electron-hole pairs in the diamond. The current through a DRD is linear in the applied bias voltage and incident photon power [20]. A bias voltage is applied with a bias tee (Figure 3.4b) that contains a series inductor and a capacitive coupling to hold charge (response time of ∼35 ps [21]). DRDs will be useful to obtain time-resolved measurements of the radiation environment. The disadvantage is the spatial resolution is limited by the packing fraction of the DRDs. We are have built our own assemblies for mounting the diamond and the closest packing distance that can be achieved given our current assembly size is ∼8mm.

3.4.2 PIN Diodes

A silicon PIN diode is formed by an intrinsic layer sandwiched by p-type and n-type on each side. Incident radiation generates electron-hole pairs in the intrinsic region and the movement of these pairs out of the intrinsic region forms the measured photocurrent. PIN diodes are cheap to obtain but suffer from a rise time that is a couple orders of magnitude larger than that of the DRD (∼10 ns vs. ∼200 ps) in addition to a longer (∼50 ns) RC-like decay [16, 18]. This time response is a function of the electron and hole mobility as well as the capacitance of the intrinsic region [20]. Given the time resolution we require in our measurements of the soft X-rays, a PIN diode does not seem to be a good candidate.

Figure 3.5: a) Transport of radiation through a GXI. Incident radiation passes from left to right initially through a K-edge light filter to remove visible light. The X-rays are then converted by the MCP into photoelectrons that are incident upon a P-43 phosphor, converting them to photons in the visible spectrum that are transported by the FOFP and then collected by the CCD. b) diagram of the GXI developed in conjunction with colleagues at LANL [5, 24, 25].

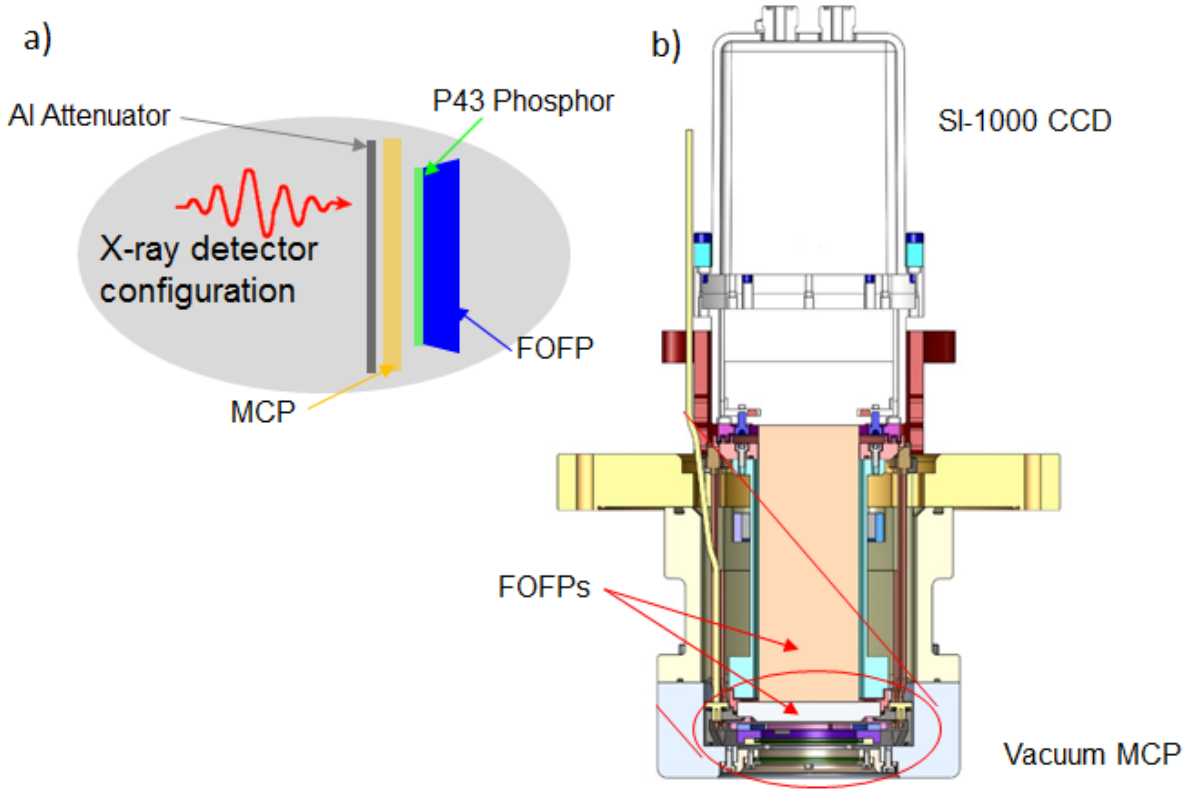

3.4.3 Gated X-ray Imager

A GXI is a composite diagnostic consisting of the pairing of a microchannel plate (MCP) with a charge-coupled device (CCD). Shown in Figure 3.5 is a current GXI build in collaboration with another group at LANL that will be used to measure the spatial and energy distribution of scattered photons along DARHT Axis-I [22]. Initially, a spatial distribution of X-rays is incident upon the vacuum MCP. The radiation passes through the MCP and is converted into visible photons by a phosphor which is then passed through a fiber optic faceplate (FOFP) to transmit the image to the CCD. A GXI has the advantage of being able to measure the full energy spectrum (if coupled with a diffractive element) and spatial distribution at a single instant of time. Resolution typically achievable in a GXI is on the order of $\sim$10 μm/pixel [22, 23].

Chapter 4

Geant4 Monte Carlo Simulations

The simulations presented in this paper were performed by a colleague at LANL, John Perry, using the Monte Carlo (MC) code Geant4. Geant4 specializes in particle transport and interactions with matter [26]. MC codes are complete in their treatment of the physics present in the system under consideration. They can handle arbitrary geometries and are easily parallelized as they are linear in processing. Each dataset (24 total) took approximately 5 hours to run on a computing cluster containing 40 CPUs.

The Geant simulations presented henceforth were given the initial conditions of a monoenergetic electron beam containing 10^9 electrons at 19.8 MeV interacting with a thin metal foil. The materials considered thus far are 100-μm-thick Ti, Cu, and Ta, in addition 1mm-thick Ta. The simulations were performed over three different energy ranges with three different bin sizes for the scattered X-rays and electrons: (1) 0–10 keV with a 10 eV step; (2) 0–100 keV with a 100 eV step; and (3) 0–20 MeV with a 20 keV step. The polar angles range from 0–360 degrees and were discretized in the simulations from 0.5 to 359.5 degrees with a 1 degree step. It is important to note that the number of electrons contained in a DARHT Axis-I pulse is $8.49 \cdot 10^{14}$, whereas the data presented are representative of the lower (10^9) electron count. It is assumed that, for the scattered X-rays, the count will scale linearly with the number of electrons in the beam pulse. We can confirm this by a spatial mapping of the

Bremsstrahlung, which is a part of the plan for future studies on Axis-I.

4.1 X-ray Spectra of Interest

Table 4.1: Characteristic K-shell spectra of Ti, Cu, and Ta from theory and their corresponding bin locations in the Grant4 simulations [11]. **These K-α_1 and K-α_2 lines are not resolved in the 0–100 keV energy range due to the large bin size of 100 eV.

Values from XDB	K-α_1 (eV)	K-α_2 (eV)	K-β_1 (eV)
Ti (Z=22)	4510.84	4504.86	4931.81
Cu (Z=29)	8047.78	8027.83	8905.29
Ta (Z=73)	57532	56277	65223
Geant4 0-10 keV	K-α_1	K-α_2	K-β_1
Ti	4515	4505	4935
Cu	8045	8025	8905
Ta	- - -	- - -	- - -
Geant4 0-100 keV	K-α_1	K-α_2	K-β_1
Ti	4550**	4550**	4950
Cu	8050**	8050**	8950
Ta	57550	56250	65250

The K-shell spectra considered in for each material are listed in Table 4.1. The primary reference for the calculations as well as the simulation is the X-ray Data Booklet (XDB) from Lawrence Berkeley National Laboratory [11]. Another well-known X-ray database is the Livermore Evaluated Atomic Data Library (EADL), which was used for the first batch of simulations as it is the default library for Geant. Interestingly, there is an energy discrepancy between these libraries. It is beyond the scope of this paper to discuss this difference, so I will dismiss it without further comment. I have included in Table 4.1 the energies of the K-line for each material from the XDB [11] and their corresponding binned locations in the 0–10 keV and 0–100 keV energy ranges. Due to the discretized nature of the simulations, we cannot resolve with current simulations the K-α_1 and K-α_2 lines of Ti and Cu in the 0–100 keV energy range. In the following sections, I will detail how I was able to get around that problem to get a representative population of the K-lines to compare against the background. The proof-of-principle measurement laid out in this paper may help to address which database is

Figure 4.1: Polar plot of the K-α_1 lines of Ti (blue), Cu (red), Ta (yellow), and 1-mm-thick Ta (purple). Energies can be found in Table 4.1. The radial scale is logarithmic and gives the count of the K-α_1 at any given location. The spectrum is only shown from $0 - 180°$ as it is symmetric in rotation about $\hat{z}$, where 0° corresponds to the direction of propagation of the beam ($\hat{z}$).

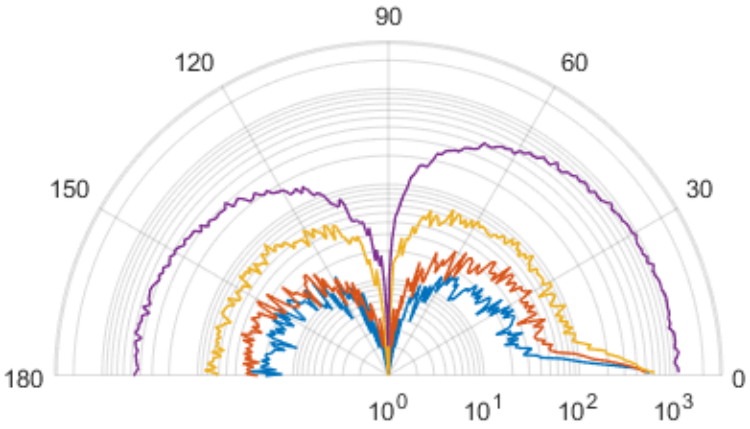

more correctly assessed and can help guide further X-ray measurements at our facility. All simulation results presented are using the XDB values of K-line energies.

4.2 Bremsstrahlung & Scattered Electrons

Collisional heating of materials with relativistic electrons will produce a continuum of both Bremsstrahlung radiation and scattered electrons. The key to successfully deploy the soft X-ray spectrometer and measure the K-lines emitted by the warm dense plasma is to characterize the polar distributions of the (1) K-lines, (2) Bremsstrahlung, and (3) scattered electrons. Each of these parameters have a clear dependence on the Z and the thickness of the foil in question, which makes material choice and target geometry a critical first step toward designing a useful soft X-ray spectrometer.

We have a range of foils available from low to high–Z. The ones in which we are currently most interested are Ti (Z=22), Cu (Z=29), and Ta (Z=73). It is trivial that the K-line energies are independent of foil geometry as they are an intensive property of the atom under consideration. However, the count of the emitted K-lines increases with both Z and foil thickness (Figure 4.1). The Bremsstrahlung energy range considered for each material

Figure 4.2: a) Polar plot of integrated Bremsstrahlung for 100-μm-thick Ti (blue), Cu (red), Ta (yellow), and 1-mm-thick Ta (purple), where the radius is the logarithm of the count. b) Plot of Bremsstrahlung energy vs. the logarithm of the count at 0.5°. The peak is shifted to approximately 100 keV by increasing the thickness (*see inset*). The total count (obtained by integrating over the entire energy range) over all angles of the 1-mm-thick Ta compared to the 100-μm-thick Ta is larger by a factor of nearly 3. The dip in count for the 1-mm-thick Ta (purple) around 55 keV is characteristic of the K-edge of the material, where the generated Bremsstrahlung is reabsorbed by the Ta atoms.

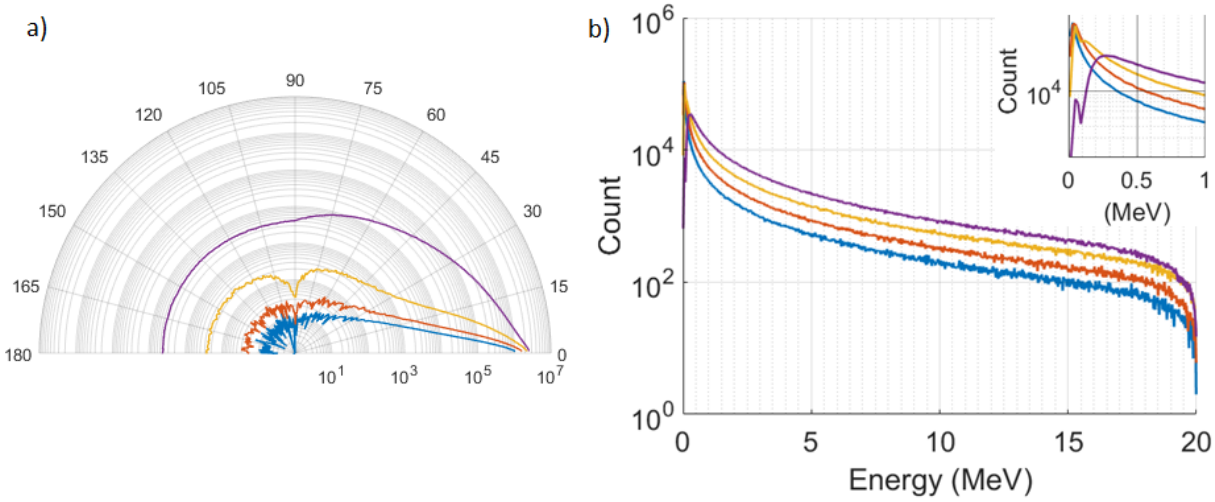

Figure 4.3: Polar plot of integrated scattered electrons from 0.01–19.99 MeV for 100-μm-thick Ti (blue), Cu (red), Ta (yellow), and 1-mm-thick Ta (purple), where the radius is the logarithm of the count. The angular distribution of this spectrum is primarily dependent on foil thickness, as a thicker foil provides a larger cross-section for the electrons to interact with the atomic lattice.

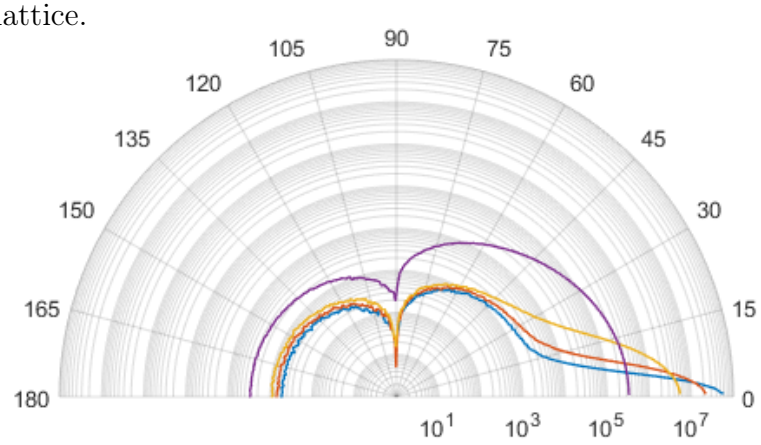

varies because of the different values for their K-β_1 lines. This defines the lower energy bound for the Bremsstrahlung whereas the upper bound at is the beam energy of 19.8 MeV which is constant across all materials. The integrated polar plot seen in Figure 4.2a is over the following ranges: Ti 0.03–19.99 MeV; Cu 0.03–19.99 MeV; Ta 0.07–19.99 MeV. The peak in energy of the Bremsstrahlung produced at the target is mostly dependent on Z, with Ti and Cu peaked at 20 keV and 35 keV, respectively. It is clear in the Ta plot that by increasing the thickness by an order of magnitude, a well-defined peak in the Bremsstrahlung energy develops around 100 keV (Figure 4.2b). The Bremsstrahlung produced from Ti, Cu, and Ta foils have high energy tails up to the electron beam energy of 19.8 MeV. To better illustrate the effect of the thickness on Ta, see the inset of Figure 4.2b. It is seen that the polar intensity of the scattered electrons increases with foil thickness (Figure 4.3).

The polar distributions for all three cases are anisotropic and have larger counts in the forward-scattered direction. The K-lines form two rather uniform hemispheres that tend to zero at 90°, but both the Bremsstrahlung and scattered electrons are much more strongly forward-scattered within a $\sim 15°$ cone about the electron beam direction of propagation. The count for the scattered Bremsstrahlung according to [7] should tend toward zero when orthogonal to the direction of propagation, but this is not observed in our simulations. It

is seen that only the K-lines tend to zero in the orthogonal direction whereas the scattered electrons and, to a lesser extent, the Bremsstrahlung, still have a significant count, especially at higher Z. Given these plots, it is in our interests to obtain simulations of the low–Z materials of varying thicknesses to observe the scaling in the count of the K-lines and Bremsstrahlung.

Scattered electrons are of less concern for our design space as we have designed and built permanent dipole magnets that can be paired with the spectrometer (i.e. crystal and detectors) to deflect electrons across all energies at which they are generated. Of paramount concern is decreasing the count of Bremsstrahlung, especially those with energies $>$ 100 keV that cannot be effectively shielded. In the following section, I will present the story of the 100-μm-thick Ti foil and use the results as a basis for the spectrometer geometry and proof-of-principle measurement of its K-α_1 line.

Figure 4.4: a) Geant4 0–10 keV polar plots of 100-μm-thick Ti K-α_1, K-α_2, and K-β_1 lines, where the radius is the logarithm of the count. b) Geant4 0–100 keV polar plots of Ti where the K-α line as a summation of the K-α_1 and K-α_2 line, with the K-β_1 line unchanged, where the radius is the logarithm of the count. Numerically adding the two lines from the 0–10 keV range shows that it matches the composite line in the 0-100 keV range.

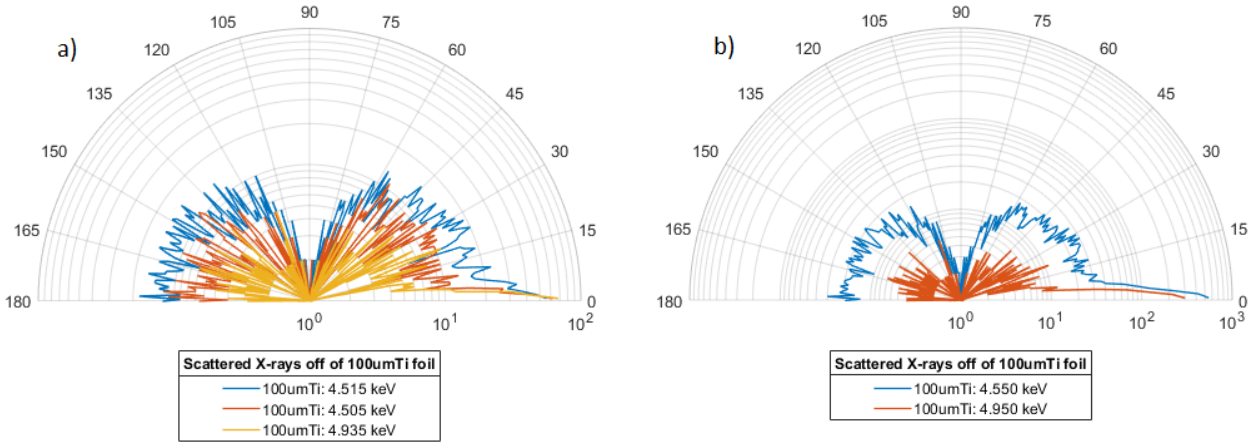

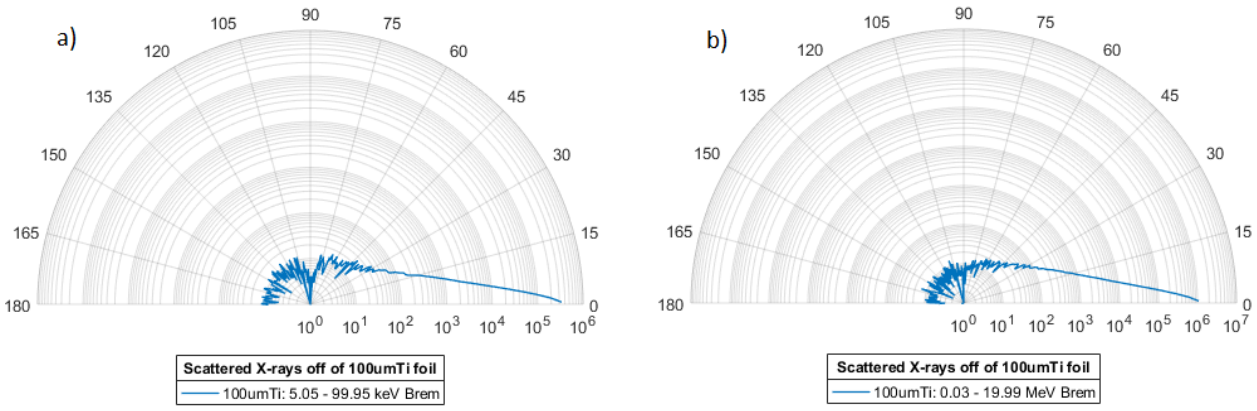

Figure 4.5: a) Geant4 0–10 keV integrated polar plot of scattered Bremsstrahlung off of a 100-μm-thick Ti foil. b) Geant4 0–100 keV integrated polar plot of scattered Bremsstrahlung off of a 100-μm-thick Ti foil. It is apparent, by directly comparing the counts between these two plots, that the majority of the scattered Bremsstrahlung energy lies below 100 keV.

4.3 Ti Spectra Analysis

Titanium has a K-edge of 4510 eV, defined by its K-α_1 line (ref. Table 4.1). We can observe the K-α_1, K-α_2, and K-β_1 lines by performing an energy lineout of the 0–10 keV dataset using the respective energies of the previously mentioned lines (Figure 4.4a). Unfortunately, the larger binned dataset cannot resolve the K-α_1 and K-α_2 lines and displays instead the sum of the two in the 4.55 keV bin (Figure 4.4b). We can directly map the counts between the 0–10keV and 0–100keV datasets. The 0–10 keV range will yield the ratio of K-α_1 to K-α_2, the sum of which is the count in the 0–100 keV range.

X-rays with energies greater than the highest energy K-line (K-β_1, 4931 eV) will constitute our Bremsstrahlung continuum. In the simulations, this corresponds to energies greater than 5.05 keV in the 0–100 keV simulation, and energies greater than 0.03 MeV in the 0–20 MeV simulation. The reason why low-Z is preferred over high-Z material is evident in Figure 4.5. We see that there is no significant contribution of Bremsstrahlung with E >> 100 keV, as evident by the similar counts from the 0–100 keV range (4.5a) and 0–20 MeV range (4.5b). This is important because it illustrates the potential to measure back-scattered K-lines amongst relatively lower energies of Bremsstrahlung.

As we have previously seen, the backscattered spectrum of both Bremsstrahlung and

Figure 4.6: a) Overlaid integrated polar plot of Bremsstrahlung (blue) and scattered electrons (red) from a 100-μm-thick Ti foil. b) Close-up image of the backscattered portion of the Bremsstrahlung and electrons. Note: this image was rotated CCW by 90° so that the electron beam direction is now vertical. This large count of scattered electrons advocates for the use of a dipole to deflect electrons.

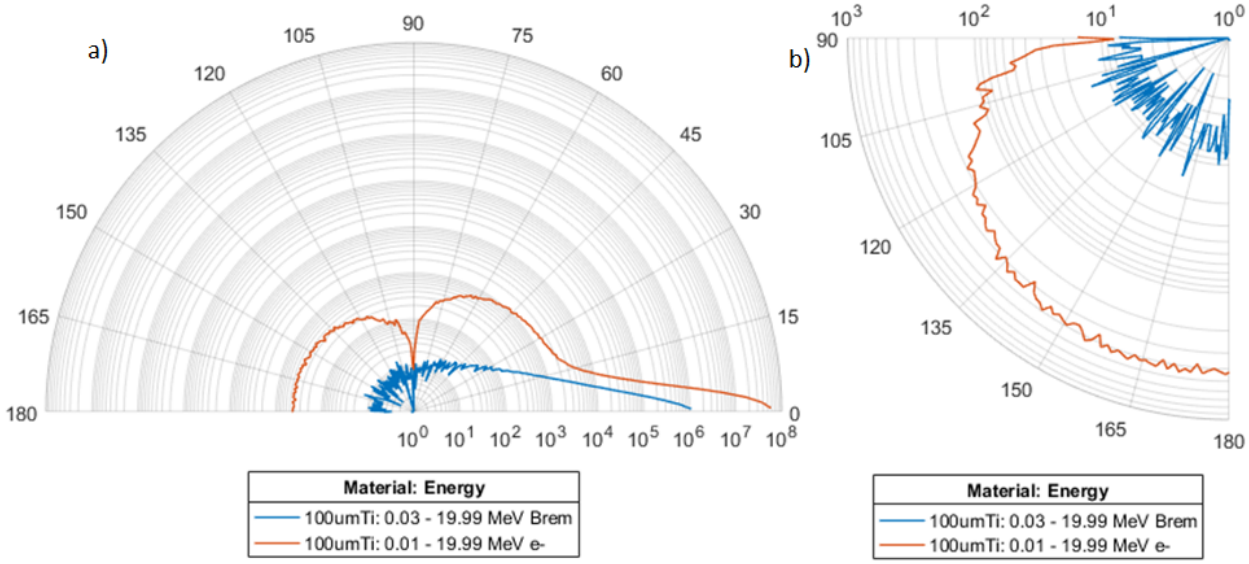

Figure 4.7: Signal-to-Noise (s/N) plot of the K-α_1 line of 100-μm-thick Ti against the background Bremsstrahlung (5.05–99.95 keV). Shown in dotted blue is the raw calculated data. The solid red line corresponds to MATLAB's native smoothing routine. The solid blue line is a manual smoothing performed by averaging over 3° increments. This poor S/N ratio advocates the need for a reflection-type geometry in the back-scattered region ($90 - 180°$).

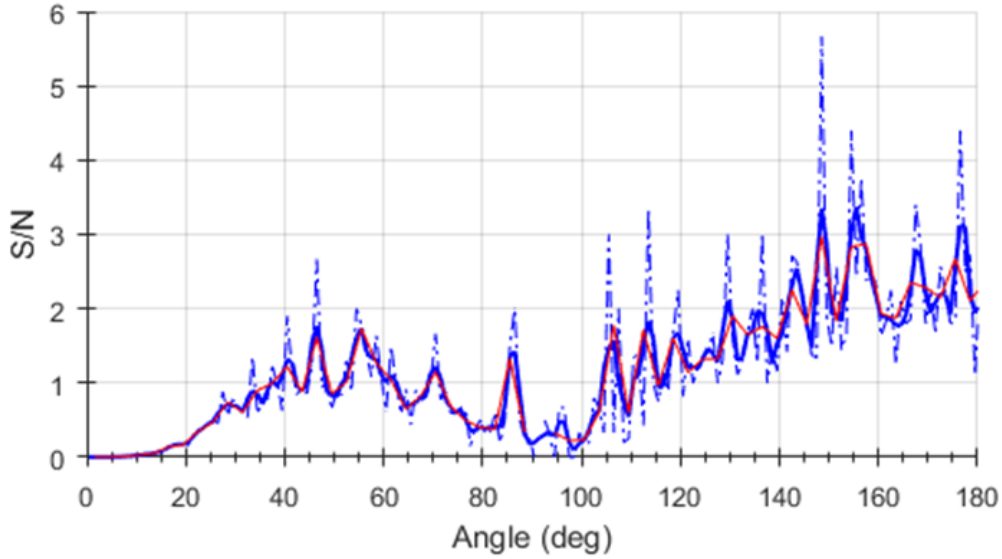

electrons is less than that of the forward-scattered. Figure 4.6 plots the Bremsstrahlung distribution on top of the scattered electron distribution. For 100-μm-thick Ti, approximately 25% of incident electrons are scattered. It is apparent that the scattered electrons dominate, but can be easily mitigated by deploying a permanent dipole magnet to deflect electrons from the detector and chosen type of diffraction mechanism. Figure 4.7 is a S/N plot of the Ti K-α_1 line against the background Bremsstrahlung. The poor S/N ratio for the K-α_1 across all angles eliminates the possibility of being able to measure any of the K-lines directly against the background as we would require a S/N $\geq$ 10. However, the lower backscattered count and slightly higher S/N opens the possibility for a Bragg spectrometer geometry. The development of the spectrometer geometry, DRD calibration studies, and the layout for the proof-of-principle measurement are the focus of the following chapter.

Chapter 5

Preliminary Design

Chapter 3 was an overview of the various spectrometers and detection techniques that have been deployed to characterize X-ray spectra from laser-driven and pulsed power-driven plasmas at facilities like NIF, Omega laser, and Sandia's Z-machine. Here, I will attempt to coalesce the knowledge gained from both proceeding Chapters into a soft X-ray spectrometer design that can be used to make a proof-of-principle measurement to help support our simulations and determine whether or not it is feasible to invest in a full-fledged design of the spectrometer. I will (1) present the spectrometer geometry that seems the best candidate for the design space on Axis-I and the (2) required intermediate step of calibrating a set of detectors to pair with the spectrometer to (3) culminate in a layout for a proof-of-principle measurement.

5.1 Bragg Spectrometer Geometry

The most important conclusion drawn from Section 4.3 is the backscattered Bremsstrahlung has both a lower intensity and energy compared to the forward-scattered Bremsstrahlung. Unfortunately, as seen in Figure 1.3, we are limited on our choice of viewports, especially upstream of the target, where there are no line-of-sight ports available beyond those orthogonal to the target. As a result, this advocates for the use of a reflection-type geometry that

has the appropriate design to diffract the Ti K-α_1 line to one of the viewports that lie in the target plane. Further, this permits the detector to be placed in the location of both minimum intensity from both scattered electrons and Bremsstrahlung.

Figure 5.1: Top-down view of a cross-section of the DARHT Axis-I diagnostic barrel laying out the geometry of the target and viewports available in the x-z plane of the accelerator. Shown in the inset is a zoomed image of the target region that gives the rough locations of the target, Bragg crystal, and detection planes.

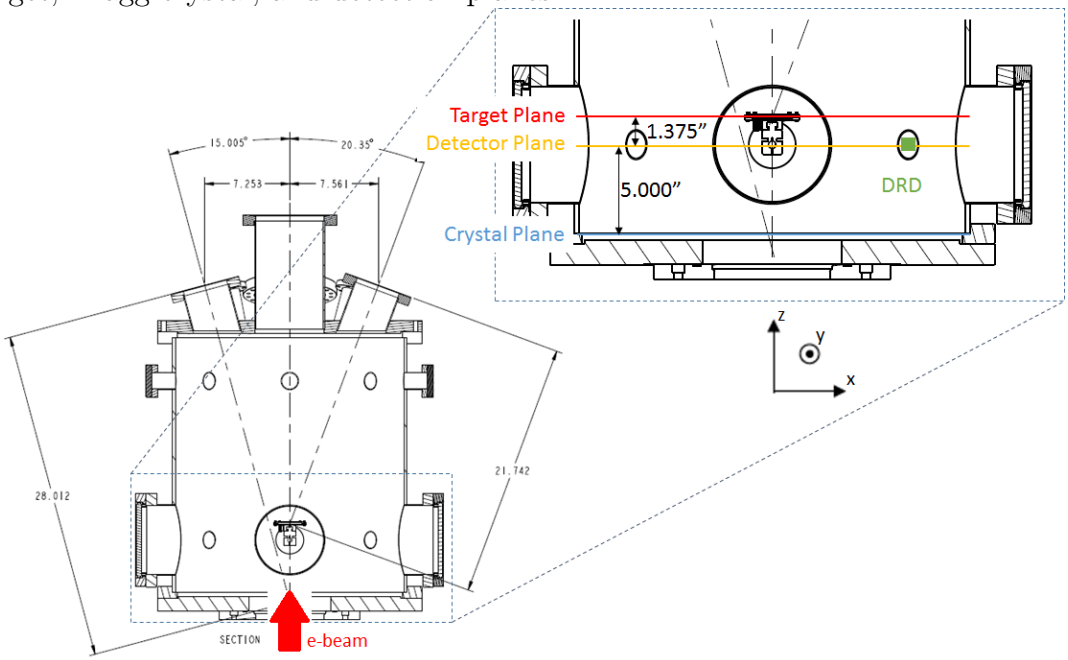

Figure 5.2: a) Top-down view of the Axis-I diagnostic barrel. b) Section A-A is a transverse cross-section of the diagnostic barrel at the center of the 6″ viewports. I have illustrated the plane in which the diffracted X-rays will lie. The DRD will be mounted in the south-west 1.5″ viewport.

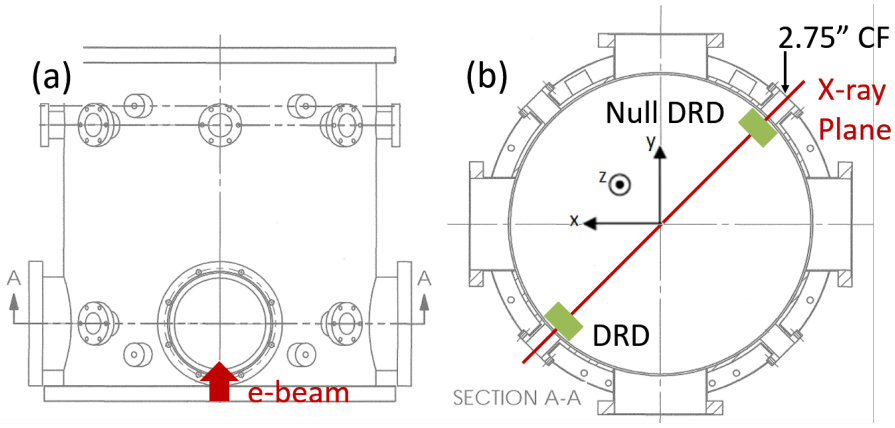

Figure 5.1 shows a top-down view of a cross-section of the DARHT Axis-I diagnostic barrel. The barrel has an internal diameter of 19.50″ and length 20″. In the inset, I have roughly sketched out here the various transverse (and orthogonal) planes in which the target, Bragg crystal, and DRD lie. The target is located 6.375″ downstream from the barrel's front inner wall, whereas the DRD is centered inside the 1.5″ diameter tube of the 2.75″ ConFlat (CF) flange viewport. Figure 5.2a is the top-down view of the barrel. In Figure 5.2b, we are examining the A-A cross-section where the electron beam is propagating out of the page. I am unable to use the 8″ CF flanges located cardinally about the beam axis because they are already used for the visible diagnostic suite (see [2] for the full visible diagnostic suite capabilities and layout). Instead, I will use one of the 2.75″ CF flanges which defines our X-ray plane as shown in Figure 5.2b. However, if this proof-of-principle measurement pans out and the Bremsstrahlung is sufficiently low at 90°, we may pair the Bragg spectrometer with a GXI in an 8″ CF.

Figure 5.3: Scale mock-up of the designed generic Bragg spectrometer geometry. We will use a LiF *(200)* Bragg crystal to diffract the Ti K-α_1 line to the 1.5″ viewport where a single DRD will be placed at a distance $\mathbf{X}'$ with respect to the inner diameter of the diagnostic barrel. The yellow box marks the location of the return current rods which is the lower bound for $\mathbf{X}$. The crystal will be placed at an axial $\mathbf{Z}$ by a custom mount. A breadboard is currently being designed to be placed on the inner transverse wall of the barrel from which to hold the crystal [23]. $\Phi(\mathbf{X}')$ represents the offset from orthogonal to the beam propagation.

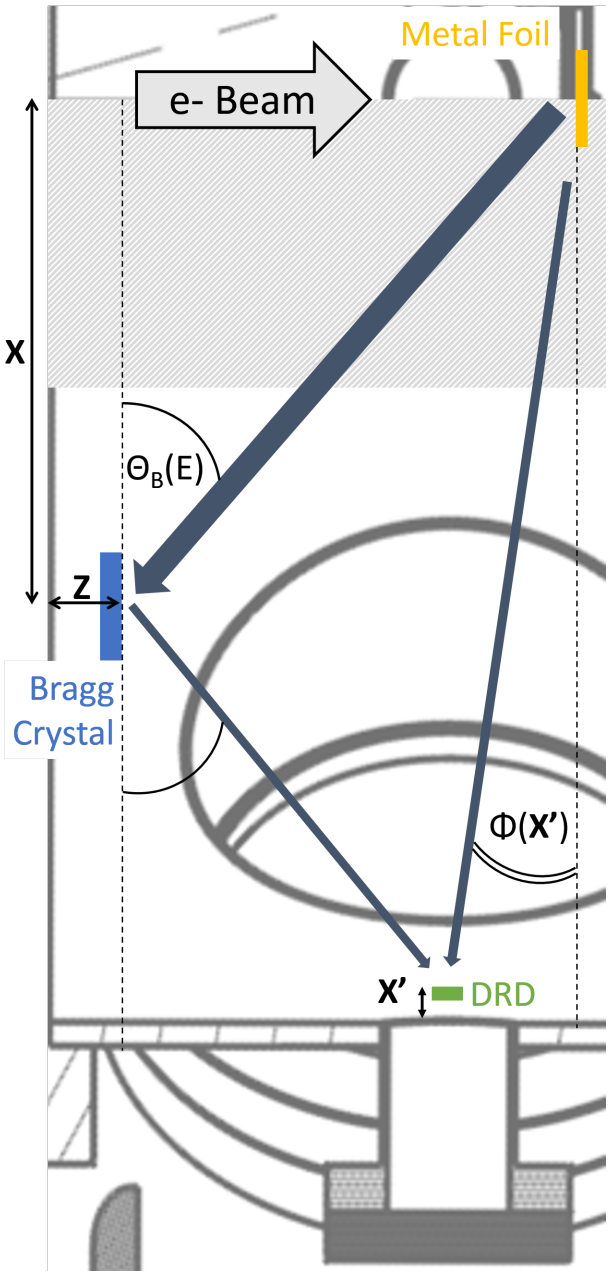

The straightforward application of Bragg's law along with basic trigonometry allows for the development of the geometry of this Bragg spectrometer seen in Figure 5.3. Here I will

give a brief summary of the methodology of the calculations. We still wish to keep the Bragg angle as close to $\Theta_B = 45°$ as possible to maximize the reflectivity of the diffracted X-rays (Section 3.3). The Ti K-α_1 line has $E = 4510eV$, which corresponds to a wavelength of 2.75Å. By using Bragg's law, $m\lambda = 2d\sin(\Theta_B)$ where m is the order of the diffracted X-ray, we can calculate the Bragg angle required to diffract this energy X-ray, provided we choose a suitable crystal. The *(200)* plane of the LiF crystal has a $2d$ lattice spacing of 4.027Å. Using this crystal, we can calculate a Bragg angle of $\Theta_B = 43.04°$, which confirms LiF *(200)* as a good choice for the range of Ti K-line energies.

The fixed variables in the spectrometer geometry include the Bragg angle, target location, and, by choice, the transverse plane in which the DRD is located. Now that we have calculated the Bragg angle, and we are given the z-locations of the target and detector (refer to Figure 5.2), we have two variables to calculate with a total of three degrees of freedom. We must determine the radial location ($\mathbf{X}$) from the center of the beamline and longitudinal distance ($\mathbf{Z}$) from the inner upstream wall of the barrel. There exists a lower bound on $\mathbf{X}$ due to the geometry of the return current rods, which are a set of 4 metal rods grounded to the beam pipe at a radius of 3″. They are required to preserve the beam's image charge and eliminate cavity modes in the change of diameter of the beam pipe from the normal 6″ along the length of the accelerator to the much larger 19.50″. $\mathbf{X}'$ is a control variable I have introduced to allow $\mathbf{X}$ and $\mathbf{Z}$ to come out to more rounded figures. Experimentally, $\mathbf{X}'$ will be the easiest to control as it can be adjusted directly by the DRD's connection through the 2.75″ CF flange. With an $\mathbf{X}' = 0.75''$, we obtain: $\mathbf{Z} = 1.50''$, $\mathbf{X} = 5.25''$, and $\Phi(0.75'') = 8°$ when rounding the actual values to clean numbers giving an acceptable error of $< 1\%$ for all variables.

Figure 5.4: a) Raw waveform from a DRD with no target installed. The off-energy electrons present at the head and tail of the beam are poorly transported throughout the accelerator and scrape the beampipe, generating Bremsstrahlung radiation that is measured by the DRD. b) Geometry of the calibration stand that holds 3 DRDs in a uniform linear orientation with 0.5″ spacing. c) Diagnostic chamber showing the placement of the calibration stand centered at one of the 8″ CF flanges located 15° from the beam direction of propagation.

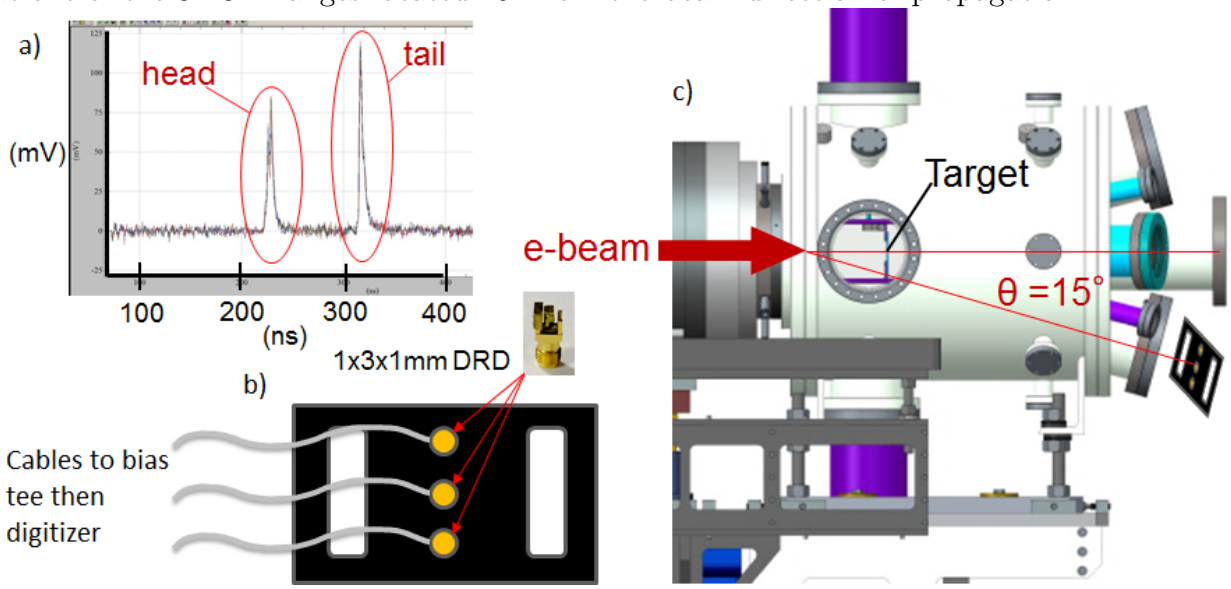

5.2 DRD Calibration Studies

Two DRDs calibrated to one another are required to perform the proof-of-principle measurement. The focus on this section is to present the methodology used to calibrate DRDs. I will elaborate on why two are needed in the following section. The signal I am measuring with the DRDs is the X-rays generated by the scraping of the electron beam off the beam pipe. Specifically, these off-energy electrons are located at the head and tail of the beam, which correspond to the rise and fall of the beam current about the flattop (at the nominal current of 1.7 kA). Figure 5.4a gives a sample signal observed on a DRD without a target installed. Here, unfocused refers to the DT1 magnet (focusing solenoid, Figure 1.3) transporting the beam through the diagnostic chamber without a target present.

I constructed a simple diagnostic that consisted of a stand to hold a set of three DRDs with a uniform orientation at a vertical spacing of 0.5″. Figure 5.4b shows the face-on view

of the calibration stand. It was located at the center of one of the 8″ CF angled 15° below the electron beam direction of propagation, as seen in Figure 5.4c. With this geometry, the upper, middle, and lower DRD are located at 14°, 15°, and 16°, respectively, off axis from the electron beam. As we shall see, even this 1° difference between detectors is enough to be observed in the measured waveforms.

Figure 5.5: a) Waveform of DRD #8 from shots 24132–24134 in the upper location of the stand. b) Waveform of DRD # 6 from shots 24135–24139 in the upper location. c) Background-subtracted and integrated voltage waveforms. It is clear that these two DRDs need calibration due to the mismatch in waveform integrated voltages.

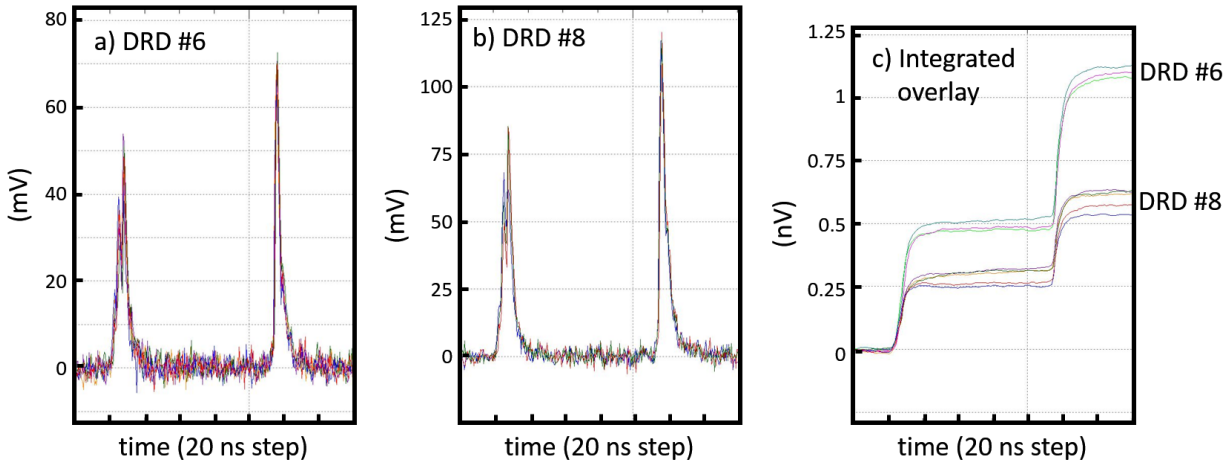

On average, at least three shots were taken for each set of data for repeatability and confidence in the measurements obtained. The data shown in Figure 5.5 was obtained by comparing the waveforms from two different DRDs from two different groupings of shots in the same location. The arrangement used here had DRD #8 in the upper location for shots 24132–24134 and DRD #6 in the upper location for shots 24135–24139, both of which are 2x3x1-mm DRDs. There are two different ways to proceed from here with the calibration. The most direct way is comparing the background-subtracted waveforms of each DRD in Figure 5.5a and b, or numerically integrate the signal to give a plot as seen in 5.5c. This second method is much easier to visually interpret, though it relies more heavily on how well the background-subtraction was performed. Artifacts of this can be seen in the later-in-time

traces in 5.5c. Further, in this plot it is apparent that these two DRDs are not in calibration with one another, given the different voltages achieved through the integration.

Figure 5.6: a) overlay of voltage waveforms from DRDs #5, 2, and 7 in the upper, middle, and lower locations, respectively, for the slightly focused shots 24183–24185. Slightly unfocused here means the DT1 magnet operates at a current strong enough to focus the beam onto the metal foil but not to the extent to produce WDM. This results in a creation of Bremsstrahlung across the entire beam pulse rather than just the head and tail. b) Integrated signal after baseline subtraction for all three DRDs. This plot illustrates the DRD's sensitivity in easily detecting the change in Bremsstrahlung at 1° increments.

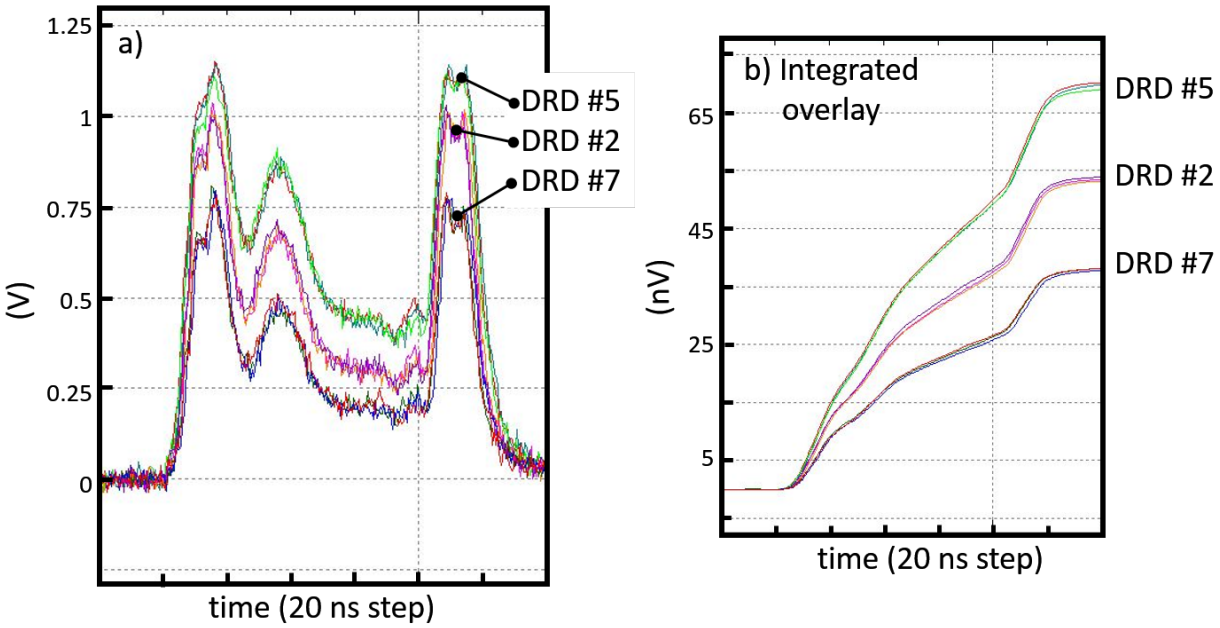

A second sample set of data I would like to highlight illustrates the sensitivity of DRD location to the measured intensity of the scattered X-rays. In a way, though without calibration it cannot yet be experimentally verified, the data presented in Figure 5.6 show that a properly calibrated set of DRDs can be used to map out the intensity of scattered Bremsstrahlung about the target region.

5.3 Proof-of-Principle Measurement

The previous two sections have presented a design for a proof-of-principle Bragg spectrometer located upstream of the target and downstream DRD measurements of Bremsstrahlung. This spectrometer has been designed around the Ti K-α_1 line and a LiF *(200)* Bragg crystal. To realize this measurement, a set of two DRDs calibrated to one another must be used, with one located according to Fig. 5.3 to measure the diffracted K-α_1 and another located at the port directly opposite to serve as a null measurement. Each DRD as well as the crystal will be paired with a permanent dipole to prevent electrons from confounding the measurement.

Figure 5.7: Close-up image of the DRD location in the barrel from Fig. 5.3. With the parameters calculated using the Ti K-α_1 and the LiF *(200)* Bragg crystal, it may be possibly to insert shielding to protect the DRD from the line-of-sight radiation. Regardless, a permanent dipole will need to be paired with the DRD to prevent the electrons from confounding the measurement.

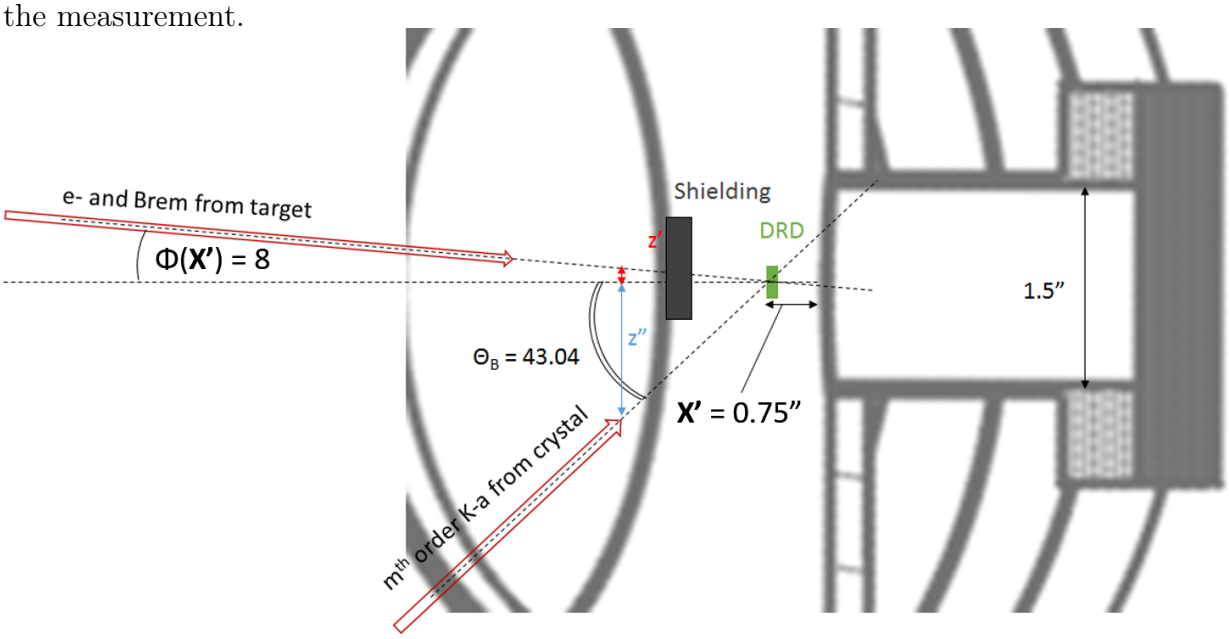

Shielding of the DRDs from the line-of-sight of the metal foil is also a possibility. The values obtained for z' and z'' are $0.14''$ and$0.93''$, respectively at a distance of $1''$ from the face of the DRD. For example, a $1''$ square piece of thin ($\sim$1mm) W can be placed here to effectively block Bremsstrahlung $<$2MeV (less than 1% transmission) and scattered electrons [27]

(see Figure 5.7). The DRD calibration studies, though incomplete and ongoing, emphasize the importance of the DRDs being located at the same angle with respect to the target, as even a minor shift of 1° can be seen in the output waveforms. A successful measurement will yield a waveform from the DRD paired with the crystal larger than that of the null DRD. It is also possible that, due to the excellent response time of the DRDs, a time evolution in the emitted lines will be discerned. The results of this measurement will help guide further development of this soft X-ray spectrometer into a full-fledged design that will be able to measure reliably the temperature and density of the warm dense plasma.

Chapter 6

Conclusions & Future Work

The goal of this project is to provide a preliminary design for an X-ray spectrometer that will measure soft X-rays in the energy range of 1–10 keV to assist in benchmarking EOS and hydrodynamic expansion models for the WDM regime. These X-rays are emitted by a warm ($T_e \geq 1$ eV) and dense ($n_e > 10^{22}$ cm^{-3}) plasma generated through a collisional heating mechanism by an intense relativistic electron beam. Fielding this soft X-ray spectrometer on DARHT Axis-I is difficult because of the high energy (up to 20 MeV) Bremsstrahlung radiation present during the beam pulse. The first required step to achieve the ultimate goal of measuring T_e and n_e is the mapping of the polar distributions of the K-lines, Bremsstrahlung, and scattered electrons for various materials. I have presented a series of simulations that have guided the development of a proof-of-principle design to measure the K-α_1 line emitted by a Ti foil. This diagnostic and measurement will be fielded soon and will guide the future design of this spectrometer. Simulations of additional target thicknesses for Ti, Cu, and other low-Z materials will be performed. These measurements will provide a detailed understanding of the time evolution of WDM and possibly improve radiographic quality at DARHT.

Bibliography

[1] *Tested by Fire – How two recent Wildfires affected Accelerator Operations at LANL.* Available at: http://permalink.lanl.gov/object/tr?what=info:lanl-repo/lareport/LA-UR-12-23713

[2] J.E. Coleman et al., "WDM experiments at DARHT," LA-UR-16-24259.

[3] R.P. Drake and P. Norreys, "Focus on high energy density physics," New J. Phys. **16**, 065007 (2014).

[4] A.B. Zylstra et al., "Measurement of Charged-Particle Stopping in Warm Dense Plasma," Phys. Rev. Lett. **114**, 215002 (2015).

[5] J.E. Coleman et al., "An optical diagnostic suite for probing WDM produced by relativistic electrons," LA-UR-15-23914.

[6] J.E. Coleman and J.P. Colgan, "Collisional heating and adiabatic expansion of WDM with intense relativistic electrons," (unpublished).

[7] M.J. Berger and S.M. Seltzer, "Bremsstrahlung and Photoneutrons from Thick Tungsten and Tantalum Targets," Phys. Rev. C **2**, 621–631 (1970).

[8] K. Moy, I. McKenna, T. Keenan, and M. Cuneo, "Time-resolved hard x-ray spectrometer", DOE OSTI, DOE/NV/11718—1280 (2006).

[9] *Henke Tables* (Center for X-ray Optics, Advanced Light Source, Lawrence Berkeley National Laboratory, 2009). Available at: http://henke.lbl.gov/optical_constants/filter2.html

[10] I. V. Khutoretsky, "Design of an optimal Ross filter system for X-ray spectra measurements in the range of 8.98-88 KeV", Rev. Sci. Instrum., **66**, 773 (1995).

[11] *X-ray Data Booklet* (Center for X-ray Optics, Advanced Light Source, Lawrence Berkeley National Laboratory, 2009). Available at: http://xdb.lbl.gov

[12] D.B. Sinars, D.F. Wenger, S.A. Pikuz, B. Jones, M. Geissel, S.B. Hansen, C.A. Coverdale, D.J. Amplefrd, M.E. Cuneo, L.A. McPherson, and G.A. Rochau, "Compact, rugged in-chamber transmission spectrometers (7–28 keV) for the Sandia Z facility", Rev. Sci. Instrum. **82**, 063113 (2011).

[13] J.E. Seely, G.E. Holland, L.T. Hudson, C.I. Szabo, A. Henins, H. Park, P.K. Patel, R. Tommasini, and J.M. Laming, "K-shell spectra from Ag, Sn, Ta, and Au generated by intense femtosecond laser pulses", High Energy Density Physics **3**, 263–271 (2007).

[14] J.F. Seely, C.I. Szabo, P. Audebert, E. Brambrink, E. Tabakhoff, G.E. Holland, L.T. Hudson, A. Henins, P. Indelicato, and A. Gumberidze, "Hard X-ray spectroscopy of inner-shell K transitions generated by MeV electron propagation from intense picosecond laser focal spots", High Energy Density Physics **5**, 263–269 (2009).

[15] J.E. Coleman and J.P. Colgan, "A spatially and temporally resolved measurement of expanding and cooling warm dense copper," (unpublished).

[16] J.E. Coleman, D.R. Welch, and C.L. Miller, "Scattered hard X-ray and γ-ray generation from a chromatic electron beam," J. Appl. Phys. **118**, 184505 (2015).

[17] R.E. Turner, O.L. Landen, P. Bell, R. Costa, and D. Hargrove, "Achromatically filtered diamond photoconductive detectors for high power soft x-ray flux measurements," Rev. Sci. Instrum. **70**, 656–658 (1999).

[18] R.B. Spielman, L.E. Ruggles, R.E. Pepping, S.P. Breeze, J.S. McGum et al., "Fielding and calibration issues for diamond photoconducting detectors," Rev. Sci. Instrum. **68**, 782 (1997).

[19] D.R. Kania, L. Pan, H. Kornblum, R. Bell, O.N. Landen, and P. Pianetta, "Soft x-ray detection with diamond photoconductive detectors," Rev. Sci. Instrum. **61**, 2765 (1990).

[20] R.B. Spielman, "Diamond photoconducting detectors as high power z-pinch diagnostics (invited)," Rev. Sci. Instrum. **66**, 867 (1995).

[21] See http://www.tek.com/components/bias-tees for information about bias tees.

[22] J.E. Coleman et al., "Design of a paraxial inverse Compton scattering diagnostic for an intense relativistic electron beam," in Proceedings of the 2013 IEEE Pulsed Power & Plasma Science Conference (2013).

[23] J.E. Coleman, personal communications (unpublished).

[24] J.A. Oertel et al., "Gated X-ray detector for the National Ignition Facility," Rev. Sci. Instrum **72**, 701 (2001).

[25] M.B. Schneider et al., "Time-resolved soft X-ray imaging diagnostic for use at the NIF and OMEGA lasers," Rev. Sci. Instrum. **77**, 10E321 (2006).

[26] See http://geant4.cern.ch/ for more information about the Geant4 toolkit.

[27] T. Murata et al., "Optimal radiation shielding for beta and bremsstrahlung radiation emitted by ^{89}Sr and ^{90}Y: validation by empirical approach and Monte Carlo simulations," Ann Nucl Med **28**, 617 (2014).

Engineering Design

The principal goal of this research project is developing the trade space in which a soft X-ray spectrometer can be deployed to measure the temperature and density of an expanding warm dense plasma phase. As a result, design permeates this project, and the design aspects should be clear from the text.

Acknowledgments

I am very fortunate to be able to do my senior project research at LANL. This opportunity would not have been available to me if it were not for the CWRU Physics and Astronomy Club when we took a trip out to New Mexico during March 2015-16; one stop was a tour of LANL. I would like to thank the Principal Associate Director of the Weapons Program (and CWRU alum!) Bob Webster and his cohort Jon Ventura for organizing and giving the tours, which included the DARHT facility. At DARHT, I would like to thank J-1 Operations Deputy Group Leader Ed Jacquez for giving the tour as well as hiring me to work there for Summer 2016 onward. Further, I am indebted to Tim Rushenberg for escorting me all summer, J-5 Group Leader Chris Rose for assisting in my transfer from J-1 to J-5, and the rest of the J-Division employees for making me feel welcome and helping me learn much about the workings of DARHT and national labs in general. I am grateful that J-5 has agreed to support my work in the future with the possibility of doing my PhD research at DARHT. Finally, this work would have not been possible without my mentor, colleague, and friend Josh Coleman (J-5 DARHT Physics and Pulsed Power) who took me under his wing with me having no prior experience in plasma, accelerator, and beam physics and has given me the freedom to learn and test my own ideas in order to learn and do ground-breaking research.